Applied Catalysis B: Environmental 227 (2018) 123–131

Contents lists available at ScienceDirect

Applied Catalysis B: Environmental

journal homepage: www.elsevier.com/locate/apcatb

Effect of the morphology and pore structure of porous building materials on photocatalytic oxidation of air pollutants

F. Gauvin*, V. Caprai, Q.L. Yu, H.J.H. Brouwers

Department of the Built Environment, Eindhoven University of Technology, P. O. Box 513, 5600 MB, Eindhoven, The Netherlands

ARTICLE INFO

Keywords:
Photocatalytic efficiency
Nitric oxide
Pore structure
Morphology
CFD simulation

ABSTRACT

This study focuses on the effect of the morphology and the pore structure of two different porous substrates, namely wood-wool cement board (WWCB) and autoclaved aerated concrete (AAC), on the air pollutant removal efficiency by photocatalytic oxidation (PCO). Their rough surface and porous structure make them appealing choices for nitric oxide (NO) de-pollution, under indoor conditions. In-depth material characterization of the two substrates is realized in order to understand the effect of the porosity, roughness and surface area on the PCO efficiency, at different air flow rates. PCO assessment shows that both activated substrates can degrade up to 99% of NO. The morphology and pore structure analyses of the two substrates reveal that a high effective area and roughness increases the PCO efficiency and an open pore structure allows a better air flow, avoiding NO_2 release.

1. Introduction

For decades, researchers have shown that indoor air quality (IAQ) has a direct impact on human health [1]. It has been demonstrated that many hazardous substances such as combustion gases, volatile organic compounds (VOC) and respirable suspended particulates (e.g. $PM_{2.5}$, PM_{10}) are emitted from cooking, paints and resins, printers, cleaning agents, cigarette smoke or building materials [2]. With the increasing concerns about the IAQ, different methods have been developed to control and reduce the indoor pollution. Photocatalytic oxidation (PCO) of pollutants is a very promising technology which brings several advantages compared to more traditional methods like filtration [3]. First, it can degrade a wide range of pollutants such as nitrogen oxides (NO_x), sulfur oxides (SO_x) and VOC without being selective [4–6]. Furthermore, this technology has been widely studied for the past years, showing positive results under both indoor and outdoor conditions [7,8]. Finally, PCO is a cost-effective process, as currently, titanium dioxide (TiO_2) is the most used photocatalyst due to its relatively low price and wide availability [7]. It has been used for a wide range of applications such as air purification or water treatment due to its high chemical stability and low toxicity [9–11]. TiO_2 is a large bandgap semiconductor with two conventional phases, rutile and more notably anatase, with a bandgap of 3.2 eV, allowing high PCO activity under UV light [12]. However, the activity of TiO_2 under visible light is limited. Doping of TiO_2 with metal (Cu, Fe, Zn) and non-metal elements (B, C, N, O, F) decreases the band gap down to 2.1–2.6 eV, increasing its PCO activity under visible light irradiation [13,14]. Different coating methods have been developed in order to provide a homogeneous dispersion of the catalyst at the substrate's surface. Dip-coating, spin-coating and spray coating have been extensively used in many types of materials [15–18]. In addition to the photocatalyst, a number of external parameters may also influence the PCO efficiency. Previous studies have reported the effect of the pollutants concentration, relative humidity or light intensity as important factors to take into account under indoor conditions [4,19–22].

Besides, the photocatalyst substrate itself can have a significant impact on the PCO efficiency. Concrete, glass or polymers have been coated and studied under indoor conditions and they all showed very different air pollutant removal efficiencies [23–25]. However, not many studies provide information about the actual influence of the morphology of the materials' substrate on the PCO efficiency [26,27]. These studies mostly focused on the general macrostructure of the substrates, where it has only been shown that porous materials are good candidates due to their high surface area available for the photo-catalytic coating [28–30]. The roughness of the surface has also been reported as an important factor during the PCO process but no investigations about the link between pore structure and PCO efficiency have been performed yet [31]. In this study, two porous materials with different morphologies are chosen in order to provide a comparative study:

The first one, wood-wool cement board (WWCB; Fig. 1A), is a composite material made of ordinary Portland cement (OPC) and wood wool, usually spruce strands [32,33]. The processed composite has a

---

* Corresponding author.
E-mail address: f.gauvin@tue.nl (F. Gauvin).

https://doi.org/10.1016/j.apcatb.2018.01.029
Received 7 December 2017; Received in revised form 11 January 2018; Accepted 13 January 2018
0926-3373/

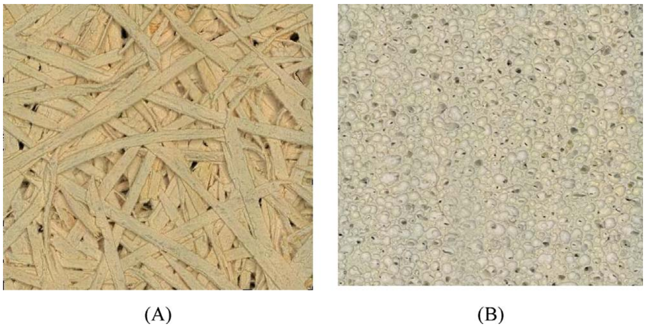

(A) (B)

Fig. 1. Picture of the two substrates. A: WWCB and B: AAC.

low density, high porosity, and shows great physical and thermal properties for various indoor applications as acoustic and thermal insulation [34–37]. The presence of wood fibers provides a heterogeneous open structure and high surface area, created by the macro porosity formed by the twine of those wood elements within the board volume [38]. These properties underline the good potential of this material as photocatalyst substrate, so far never reported in the literature.

The second one, autoclaved aerated concrete (AAC; Fig. 1B) is categorized as a lightweight concrete and is usually applied as partition wall element or supporting structure, as it ensures high thermal performances. Due to the presence of unconnected pores, these materials features are related to its closed-pore structure, created by the air voids entrapped in the cement matrix [39,40]. Moreover, the presence of the foaming agent results in a high superficial roughness, where "roughness" stands for the average depth of the pores characterizing the material substrate. Unlike WWCB, the application of AAC as a substrate for photocatalytic purposes has been investigated successfully [41,42]. Thanks to their good thermal and acoustical properties, these two substrates can be used for various PCO indoor applications, such as activated ceiling tiles or self-cleaning walls.

Despite their comparable physical properties (i.e. porosity and density), the two substrates feature very different types of pore structure. The WWCB is characterized by an open structure, which allows the air flow to pass through the matrix due to the high presence of the macroporosity. On the other hand, AAC presents a closed structure, mainly based on smaller pores, minimally connected with each other, which prevents the air flow from passing through. The presence of similar physical features of the two substrates (i.e. surface area and porosity) aims to limit the influencing variables on the PCO activity and provide a more reliable comparison among the two type of structure.

The aim of this study is to investigate the effect of the morphology of WWCB and AAC on the photocatalytic oxidation of NO under indoor conditions. Different methods have been used to study the composite structure and morphology of the two substrates, by characterizing their type of porosity, roughness and specific area and their influence on the PCO efficiency. The PCO efficiency of coated WWCB and AAC is evaluated, following the ISO 22197-1 standard, with NO selected as the target pollutant. Computational fluid dynamics (CFD) simulation is realized to study the pollutant flow across the substrate and how it influences the photocatalytic oxidation of pollutants.

2. Experimental

2.1. Materials

For the WWCB manufacture, Norway spruce strands are provided by Knauf Insulation (the Netherlands) and mixed with a mineral binder consisting of 36.63% limestone and 63.37% CEM I 52.5 R white, provided by ENCI (The Netherlands). AAC substrates are manufactured by using lime, calcium hydroxide, CEM I 52.5 R (provided by ENCI, the Netherlands), fine quartz powder, calcium sulfate and metallic Al. The recipe applied is provided by HESS AAC Systems (The Netherlands) and all the materials fulfill the recommended requirements for AAC production. KRONOclean KC 7404 is provided by Kronos International. It consists of an aqueous suspension of carbon-doped TiO_2 with a concentration of 40% (m/m). Its properties are the following: pH of 7–8 (at 20 °C), flash point > 90 °C, density of 1.35–1.55 g cm^{-3} (at 20 °C) and dynamic viscosity < 800 mPa s.

2.2. Methods

2.2.1. Substrate manufacture

WWCB substrates are manufactured by using Norway spruce strands of 1.5 mm. The dry wood has been pre-soaked with water, in order to reduce the strands brittleness as well as to provide water for the binder reaction. The dry cement is sprinkled on the wet spruce and mixed, for achieving a homogeneous binder coating. The water to binder mass ratio applied is 1, while both the wood to binder mass ratio and the wood to water mass ratio are 0.75. Then the mixture is transferred to a mold of 20 × 15 cm^2, the boards are pressed for 24 h and then cured under ambient condition, covered with a plastic sheet for 10 days. Samples are dried overnight in the oven at 50 °C prior to PCO assessment.

The AAC substrate has been produced by mixing fine quartz and portlandite powder in preheated water (45 °C) in a mixer (Swinko EZR 22R, R/L with a 4 bladed propeller mixing rod). Once a homogeneous paste is acquired, lime is added, followed by cement and anhydrite (after 30 s). Finally, metallic Al powder, premixed with 100 mL of water, is added. The casted samples are de-moulded after 12 h and hydrothermally cured (autoclave: Maschinenbau Scholz GmbH&Co., KG/steam generator: WIMA ED36) for 8 h following this procedure: 1.5 h heating, 5 h plateau at 190 °C and 11 bar, 1.5 h cooling. All the samples are cut to fit the PCO reactor dimensions (20 × 10 × 1.5 cm^3).

2.2.2. Photocatalyst coating

To ensure a homogenous dispersion of the C-TiO_2 at the samples surface, 400 ± 15 mg of KC7404 is diluted in 10 mL of water. The coating is then deposited on the surface of each substrate by spray coating at a rate of 10 mL/min, resulting in 2 mg/cm^2 of C-TiO_2 at their surface. Samples are then dried at 40 °C for 24 h in order to remove the residual moisture.

2.2.3. Particle size distribution and zeta-potential

The particle size distribution (PSD) and the zeta potential (ζ-potential) of the suspension are measured by a Malvern Zetasizer Nano ZS. Pure and diluted KC 7404 C-TiO_2 suspension are evaluated in the 50 µL polystyrene cells. Each measurement is performed 3 times at 25 °C according to the operating instructions.

2.2.4. Digital microscopy

3D surface profiles of WWCB and AAC are acquired by using a VHX 5000 series Keyence digital microscope. Samples are cut into three parts with an area of 40 × 40 mm^2, where the surface area is measured. Therefore, the value measured is the total surface per 1600 mm^2. For each material, a cross section profile drawn on the substrate surface is measured by averaging an area of 10 mm^2 on the top of the substrate, by sectioning the surface at 0.5 mm^2 intervals. In order to get an overall profile, the average of three horizontal and three vertical cross section profiles are considered to calculate the board roughness.

2.2.5. Scanning electron microscopy (SEM)

SEM analyses are performed by using a Phenom ProX scanning electron microscope to observe the surface and microstructure of samples. Micrographs are recorded by using back scattering electrons detector at 15 kV with a spot size of 4.

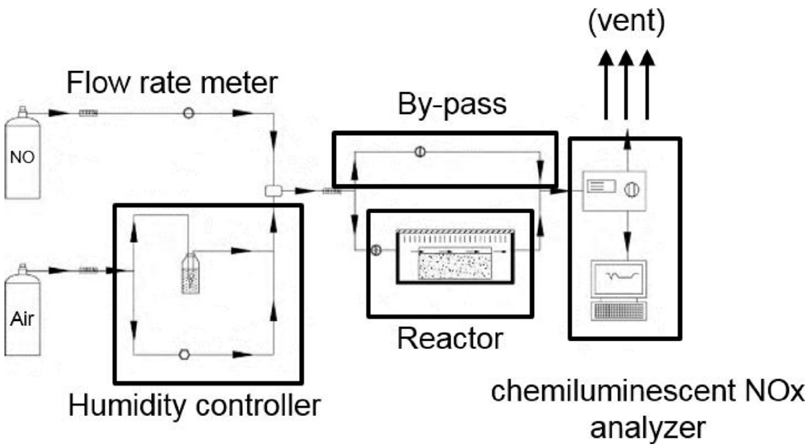

Fig. 2. Scheme of the PCO setup.

2.2.6. Energy-dispersive X-ray spectroscopy (EDX)

Energy-dispersive X-ray spectroscopy (EDX) analyses are performed by using a Phenom ProX scanning electron microscope using back scattering electrons detector at 15 kV with a spot size of 4 to study the dispersion of the TiO_2 at the surface of the sample.

2.2.7. Photocatalytic efficiency assessment

The photocatalytic efficiency of the coated samples is characterized by measuring the NO_x ($NO + NO_2$) conversion, using a plug-flow experimental setup, depicted in Fig. 2. The setup is designed using the ISO 22197-1:2016 standard as a reference, applying visible light instead of UV-A light in order to simulate indoor environment. Nitric oxide (NO) is selected as the model pollutant and flows above the substrate within a gap of 3 mm. NO gas is mixed with synthetic air to reach an inlet NO concentration of 1 ppm, and different air flows from 1 L/min to 3 L/min are applied. The emission source is composed of three fluorescent lamps of 25 W each, emitting a visible light irradiation with a wavelength of 400–700 nm and set at $10.0 \pm 0.1\ W/m^2$. A chemiluminescence NO_x analyzer APNA-370 manufactured by Horiba is used to monitor the NO_x conversion. The amount of NO_x converted in the PCO reactor is calculated following:

$$\%Conversion = \frac{[C_{NOx}]_{in} - [C_{NOx}]_{out}}{[C_{NOx}]_{in}} \times 100 \qquad (1)$$

Where $[C_{NOx}]_{in}$ is the initial concentration [ppm], measured by taking the average value of the first 5 min of the experiment, before turning on the light. The outlet concentration $[C_{NOx}]_{out}$ is measured by taking the average value of the last 5 min of the irradiation period [ppm]. Since the oxidation of NO may produce NO_2, the outlet NO_x is constituted of the remaining NO and the produced NO_2.

Several constituents are flowing through the reactor, namely NO (pollutant), $O_2 + N_2$ (gas carrier) and H_2O, since the relative humidity is set at 50%. When these three constituents are in contact with the photocatalyst, they are adsorbed on the surface of the active sites, following the mechanism described in the Eqs. (2)–(4) below [19]:

$$\text{C-TiO}_2\ \text{(active site)} + NO \rightarrow NO\ \text{(adsorbed)} \qquad (2)$$

$$\text{C-TiO}_2\ \text{(active site)} + O_2 \rightarrow O_2\ \text{(adsorbed)} \qquad (3)$$

$$\text{C-TiO}_2\ \text{(active site)} + H_2O \rightarrow H_2O\ \text{(adsorbed)} \qquad (4)$$

By visible light irradiation, the PCO process starts, generating electron/hole pairs as described below:

$$\text{C-TiO}_2 + h\nu \rightarrow e^- + h^+ \qquad (5)$$

Then holes are trapped by the water while electrons are trapped by the oxygen:

$$H_2O\ \text{(adsorbed)} + h^+ \rightarrow OH\cdot + H^+ \qquad (6)$$

$$O_2\ \text{(adsorbed)} + e^- \rightarrow O_2^- \qquad (7)$$

Finally, the formed hydroxyl radical reacts with the pollutant, oxidizing NO to NO_3^-. However, the mechanism leads to by-products such as HNO_2 and NO_2 [43]:

$$NO\ \text{(adsorbed)} + OH\cdot \rightarrow HNO_2 \qquad (8)$$

$$HNO_2 + OH\cdot \rightarrow NO_2 + H_2O \qquad (9)$$

$$NO_2\ \text{(adsorbed)} + OH\cdot \rightarrow NO_3^- + H^+ \qquad (10)$$

NO_2 can also be hydrolysed in presence of light irradiation, forming HNO_2 in the gas phase, while HNO_3 goes in the aqueous phase [44,45]:

$$2\ NO_2\ \text{(adsorbed)} + H_2O + h\nu \rightarrow HNO_2 + HNO_3 \qquad (11)$$

Moreover, electron/hole pairs may be recombined again during the process, generating heat, thereby decreasing the PCO efficiency, since it deactivates electron/hole pairs:

$$e^- + h^+ \rightarrow \text{heat} \qquad (12)$$

The NO_2 released by the NO incomplete conversion can be calculated with the yield of the chemical reaction:

$$NO + 2OH\cdot \rightarrow NO_2 + H_2O \qquad (13)$$

Moreover, it is possible that some other by-products are released in the gas phase during the incomplete conversion of NO to NO_3^-.

The reaction (13) is the combination of the Eqs. (8) and (9), showing the formation of NO_2 by oxidation of NO. Consequently, the reaction yield (Eq. (12)) shows the fraction of NO_2 formed during the oxidation process and gives a good representation of the PCO conversion rate:

$$NO_2 Reaction\ Yield = \frac{[C_{NO_2}]_{out} - [C_{NO_2}]_{in}}{[C_{NO}]_{in} - [C_{NO}]_{out}} \times 100 \qquad (14)$$

Where $[C_{NO2}]_{out}$-$[C_{NO2}]_{in}$ is the actual yield [ppm] (i.e. the amount of NO_2 formed during the reaction) and $[C_{NO}]_{in}$-$[C_{NO}]_{out}$ is the theoretical yield [ppm] (i.e. the maximum amount of NO_2 that can be formed during the reaction which is the complete conversion of NO to NO_2).

It is important to note that as described in Eq. (11), a fraction of NO_2 can be oxidised into HNO_2 and HNO_3. It means that the NO_2 concentration measured by chemiluminescence may include other by-products [45]. Since these by-products are in very low concentration, no further distinction between HNO_2, HNO_3 and NO_2 is made in this study [46].

2.2.8. Air flow simulation

The aim of this study is to simulate air flow in the reactor by CFD in order to understand the differences in behavior between the two substrates. Zhang et al. simulated by CFD the air/pollutant flow in contact

Table 1
Results of the particle size distribution and zeta potential analysis of KC7404.

Zeta potential	mV	− 32
PSD range	nm	20–400
Average particle size	nm	119
pH	–	7.2

with a different kind of roughness by designing simple 2D elements such as square, triangle, round or semi-round models on a flat surface [31]. They found that the higher the roughness, the higher the PCO efficiency.

The estimation of the behavior of the flow in the proximity of WWCB and AAC is analyzed by using Flowsquare 4.0 software. A two-dimensional model of the two substrates has been drawn, respecting the measurement and morphology characterized by digital microscopy. The CFD simulates the velocity of the flow at the entrance of the reactor and in the proximity of the substrate surface with an inlet flow of 0.06 m/s. These conditions correspond to a volume flow rate of 1 L/min, simulating the lower flow rate available for the PCO setup.

3. Results and discussion

3.1. Photocatalyst characterization

Zeta potential and particle size distribution of KC7404 are measured after dilution. Table 1 shows a summary of the results.

Pure KC7404 has a high stability, showing a zeta potential of − 32 mV. Its PSD analysis shows a distribution ranging between 20 and 400 nm, characterized by a sharp peak at 119 nm, considered in this study as the average diameter. Zeta potential is an indicator of the stability of colloidal dispersions. When the absolute value of the zeta potential is high (± 30–50 mV), dispersions are stable thanks to electrostatic repulsion between particles. On the other hand when the zeta potential is close to zero, the coagulation of particles is fast, causing formation of clusters of particles and eventually their sedimentation. Here, the zeta potential shows that the TiO_2 particles are stabilized in the solution which limits the coagulation leading to the formation of TiO_2 clusters after coating. Moreover, the PSD analysis proves the very fine size of TiO_2 which would be able to cover all the pores of the substrates.

3.2. Composite surface characterization

3.2.1. Digital microscopy

Fig. 3 shows the 3D surface profile of the WWCB and AAC (Fig. 3A and B), respectively) while Fig. 4 shows the average cross section profiles of the WWCB (Fig. 4A) and AAC (Fig. 4B). Physical properties such as roughness or surface area are calculated and displayed in Table 2.

The two materials show very different morphologies. The WWCB has randomly dispersed strands, creating open porosity with pits of significant depth (4.25 mm) in the material as well as a very heterogeneous surface, explaining the roughness of the material. Compared to WWCB, the AAC has numerous pores which are more homogeneously dispersed in the material's matrix, but with a reduced diameter (1.2 mm) and depth (0.57 mm). However, according to some studies, the surface area of an AAC's pore is significantly higher than at its surface because of the high roughness inside the pore, creating by the foaming agent [47]. In this study, the surface area of both substrates is measured by digital microscopy but this method has a resolution not high enough to detect micro pores. Therefore, it is possible that this property has been undervalued for the AAC. The density and the porosity of the two substrates are very comparable: WWCB has an apparent density of 464 kg/m^3 and porosity of 83% for WWCB, while AAC presents a density of 461 kg/m^3 and a porosity of 82%. On the other hand, the surface area of the AAC is slightly higher than WWCB, whereas the WWCB has a greater roughness. In overall, both substrates have a significantly higher surface area than the conventional flat substrate, such as glass or concrete, by a factor of approximately 1.75.

3.2.2. SEM and elemental analysis

Figs. 5 and 6 show the SEM pictures of the WWCB and AAC, respectively, while Figs. 7 and 8 their respective EDX spectra, measured at different spots, specified in the micrographs Figs. 5 and 6. Micrograph at low magnification of the WWCB shows the two constituents of the composite, namely the spruce strand and the cement layer, covering the wood wool. The overall surface of the WWCB is rough and cracks are observable at the fiber/cement interface. Two EDX analyses are performed at the cement's surface (spot 1) and at the spruce's surface (spot 2). Both EDX spectra show the presence of titanium with two peaks at 4.5 and 4.9 keV corresponding to its kα_1 and kβ_1 energy levels. This explains that the TiO_2 coating is uniform and that not only the external surface of the strands (i.e. the external surface of the composite) is coated but also spruce strands which are located inside the matrix of the composite. Considering the hygroscopic behavior of WWCB, the photocatalyst, diluted in water, diffuses inside the WWCB, reaching deeper regions inside the composite [38].

A Micrograph at low magnification (Fig. 6A) of the AAC's surface shows the macro-porosity generated by the foaming agent reaction. Two additional micrographs at higher magnification (Fig. 6B and C) are performed inside a small pore and at the bottom of a bigger pore. This result indicates the presence of a roughness on a micro scale, which is

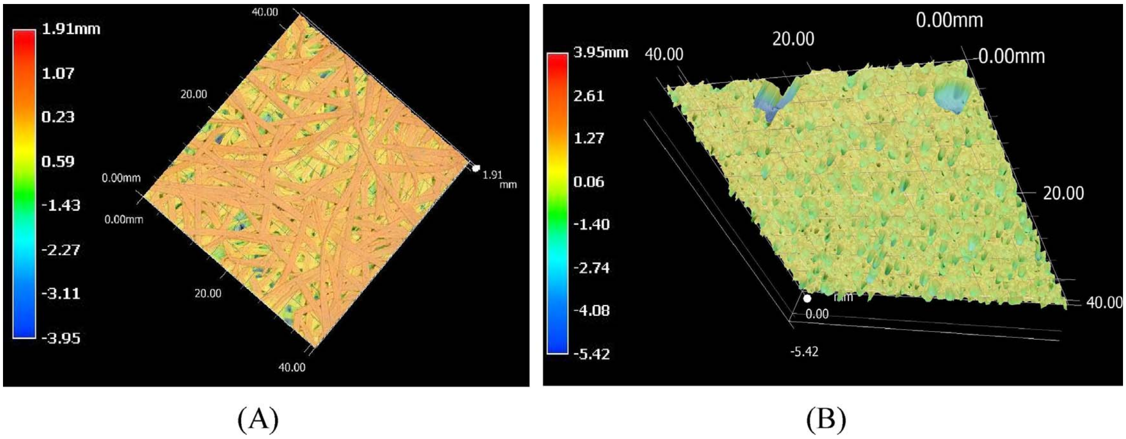

Fig. 3. Surface profile of (A) WWCB; (B) AAC. The color indicates the depth from red (shallow) to blue (deep). (For interpretation of the references to colour in this figure legend, the reader is referred to the web version of this article.)

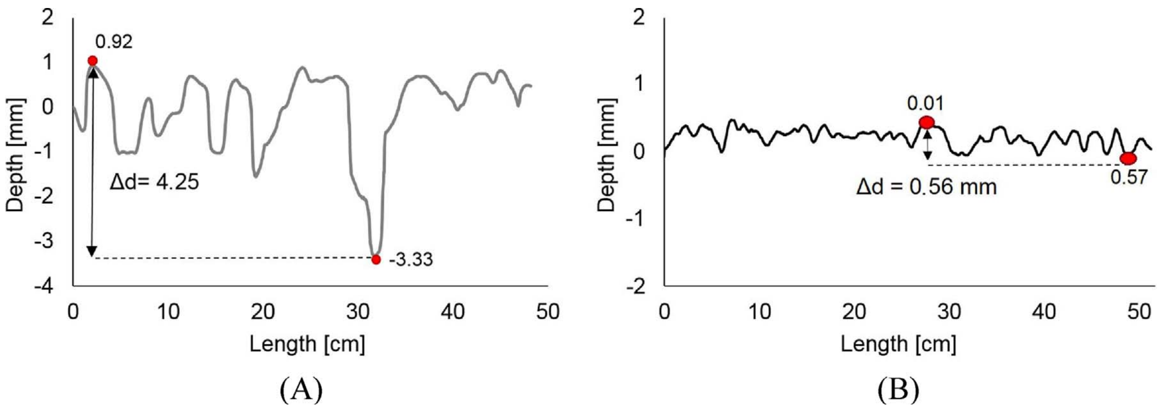

(A) (B)

Fig. 4. Cross section of the WWCB (A) and AAC (B). The profiles are the results of 12 cross sections, taken in different directions and averaged.

Table 2
Measured and calculated physical properties of WWCB and AAC.

	Apparent Density [kg/m^3]	Porosity [%]	Surface area [mm^2]	Roughness [mm]	Pits diameter average [mm]
WWCB	464	83	2795	4.3	2.6
AAC	461	82	2806	0.6	1.2

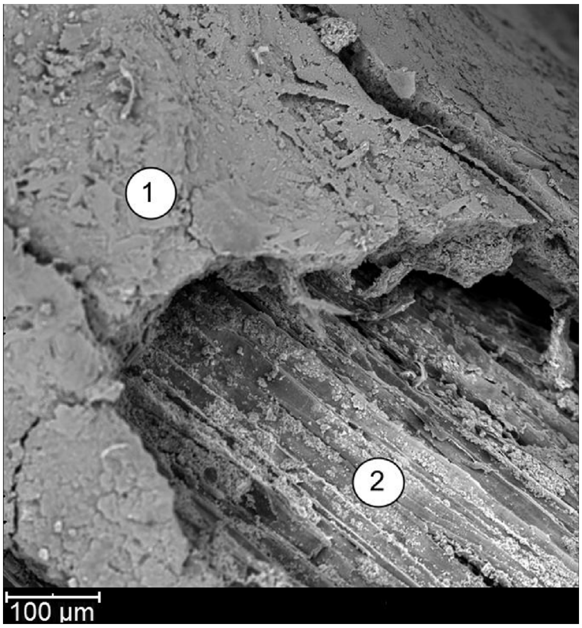

Fig. 5. SEM micrograph of the WWCB.

out of range of the digital microscope, thus was not detected.

Therefore, it is worth noting the difference between surface area and effective area: The surface area is a physical property measured by digital microscopy and refers to the substrates macro-structure whereas the effective area is defined as the surface coated by the photocatalyst and is much higher that the surface area because it includes micro-pores and micro-roughness that is not measured by the digital microscope. Thanks to the SEM analyses, it can be concluded that the surface area of the two substrates is similar but the effective area of the AAC should be much higher than the WWCB's one.

Three corresponding EDX analyses are performed at the AAC's surface (spot 1) and inside small pores (spot 2) and big pores (spot 3). Similarly to the previous observation with WWCB, the EDX spectra show the presence of TiO_2 at the AAC's surface and inside the big pore. Furthermore, even though characterized by a weak signal, a photocatalytic layer is observable even deep inside the smaller pores. Since the photocatalyst average size ($d = 119$ nm) is significantly smaller than the size of the micropores inside the visible pores ($d = 0.8$ to 2 µm) (Fig. 6B), the photocatalyst can entirely coat the surface of the pore, leading to a very high effective area of the AAC. This evidence proves that the photocatalyst is not only spread at the AAC's surface but also inside its pores, independent of the size. The efficiency of these coated parts has to be evaluated based on the air flow, as the reduced size of the pores does not ensure the presence of air flow in those areas.

3.3. Photocatalytic efficiency assessment

Fig. 9 shows the NO and NO_x degradation results of the activated WWCB and AAC, tested under visible light irradiation for a duration of 30 min at three different flow rates (1/2/3 L/min) with a relative humidity set at 50%. In overall, the NO_x degradation is affected by the pollutant flow and by the effective area of the boards. While conventional substrates such as mortar or concrete hardly degrade more than 40% of NO_x, especially at high flow rate [27,48], a very high degradation rate is observed for both substrates, where at least 80% of NO_x is converted.

Focusing on the NO results, Fig. 10 shows that the activated AAC can degrade between 98 and 95% of NO with a very small influence of the flow rate, whereas activated WWCB shows a similar NO degradation at low flow rate (98%), but lower efficiency at high flow speed (85% at 3 L/min). The small difference in surface area (2806 mm^2 and 2795 mm^2 for AAC and WWCB respectively) is not sufficient to justify such a difference in degradation rate. However, as shown in Fig. 6B and Fig. 8, the effective area covered by the catalyst counts also deep regions in these composites, not detectable by the used digital microscopy. Therefore, the difference in degradation rates is ascribable to the difference in the effective area of the substrates, higher in AAC due to the high micro porosity detected [29,30]. Besides, it is interesting to notice that the NO_x (i.e. $NO + NO_2$) degradation is very different between the two substrates. The NO_x degradation of the activated WWCB is similar to the NO degradation, while the NO_x degradation of the activated AAC is significantly lower than the NO degradation, which in this case, is strongly affected by the flow rate (95% at 1L/min to 82% at 3L/min).

These results indicate that the activated AAC has the tendency to release much more NO_2 than the WWCB, even at low flow rate. A study of the NO_2 generated by the incomplete conversion of NO displayed in Fig. 11 confirms this observation, showing the NO_2 yield as a function of the flow rate for the activated substrates. As suspected, the higher the flow rate, the higher NO_2 is released from AAC: At higher flow (3 L/min), the NO_2 formation exceeds 10%.

On the other hand, WWCB releases little or no NO_2 and it appears that the flow rate does not have an influence on the NO_2 formation. This

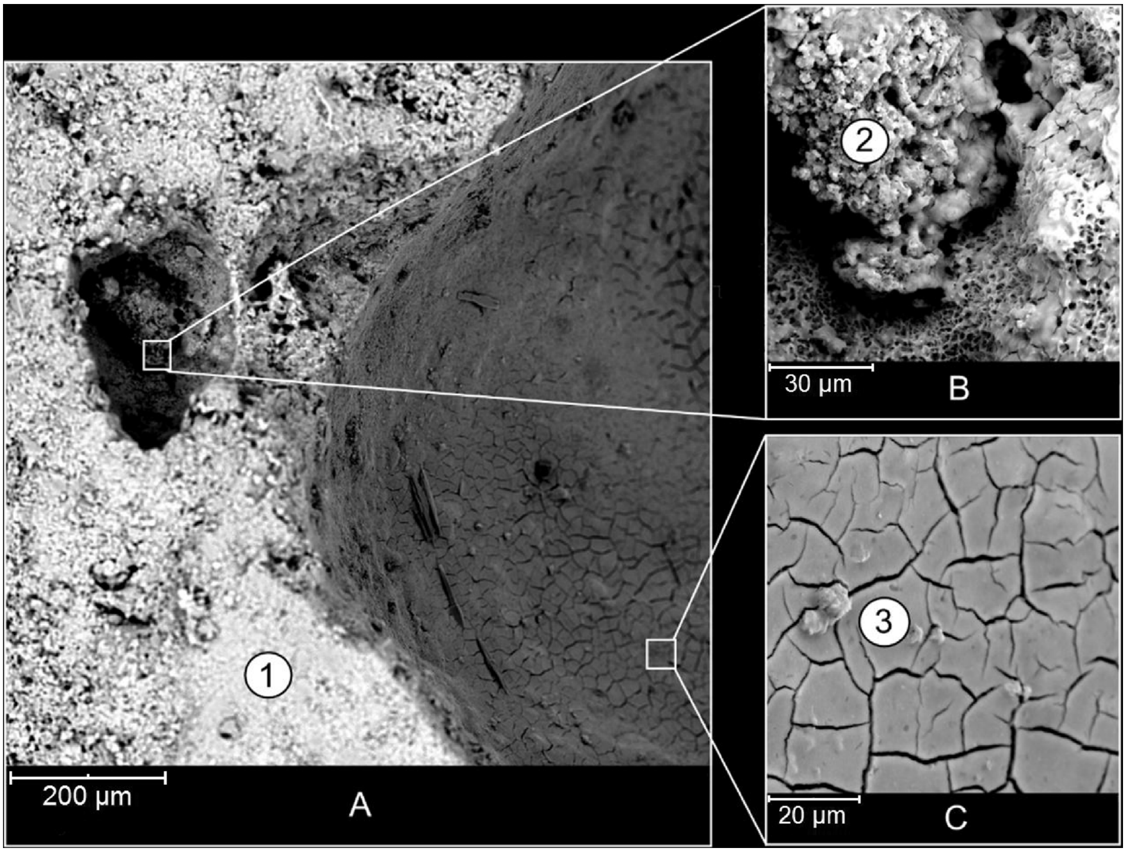

Fig. 6. SEM micrographs of the AAC. Three different areas have been analyzed: (A) The AAC's surface at low magnification; (B): Inside a small pore at higher magnification; (C) Inside a big pore at higher magnification.

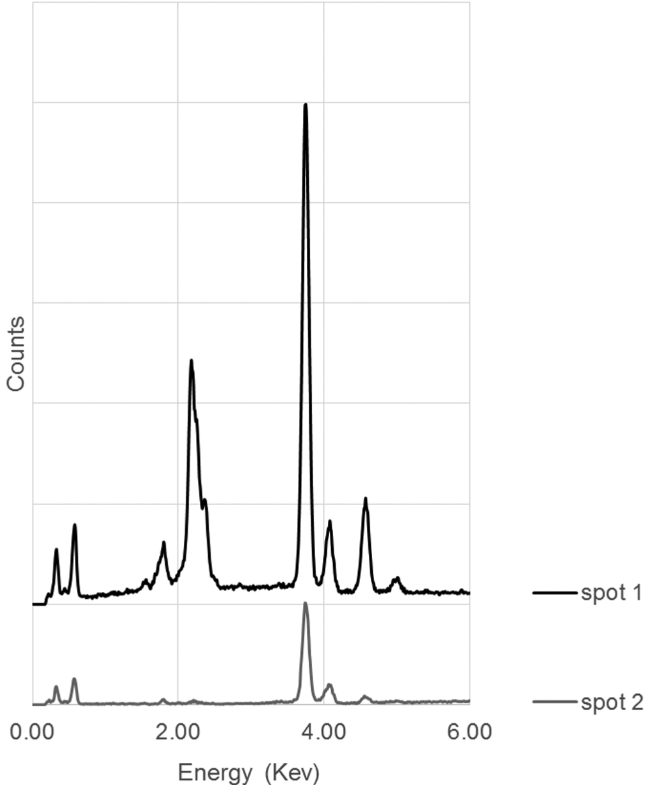

Fig. 7. EDX spectrum of the WWCB. The analysis has been done at two different spots (1 and 2) as seen in Fig. 6.

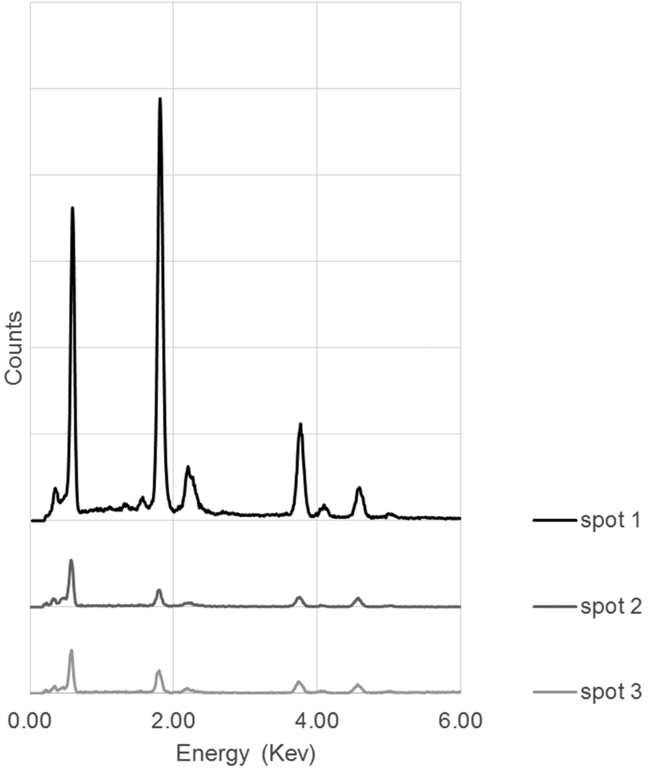

Fig. 8. EDX spectrum of the AAC. The analysis has been done at three different spots (1, 2 and 3) as seen in Fig. 7.

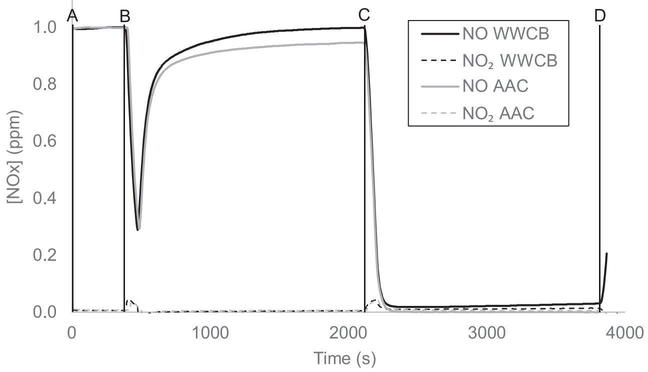

Fig. 9. Example (at 1 L/min) of the NO and NO_2 concentration development during PCO assessments. Steps are the following: A: Opening the by-pass; B: Closing the by-pass; C: Turning on the light (time = 0 min); D: End of the experiment (time = 30 min).

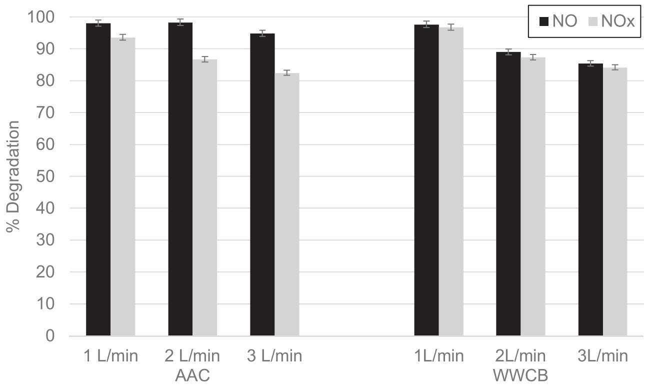

Fig. 10. The NO and NOx degradation results of the activated WWCB and AAC during the de-NOx assessment at three different flow rates (1/2/3 L/min) under visible light irradiation at 50% of re lative humidity.

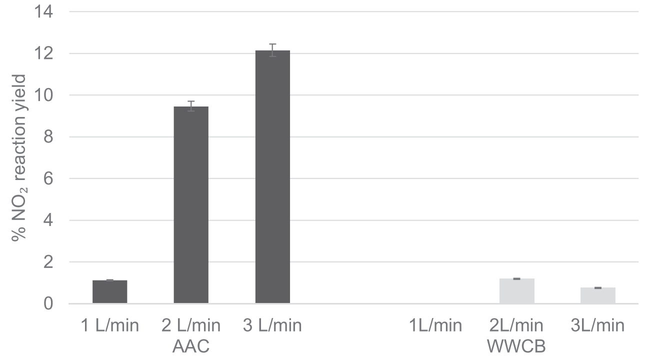

Fig. 11. NO_2 formation during the photocatalytic efficiency assessment by the activated WWCB and AAC, calculated with the Eq. (13).

very high NO to NO_3^- conversion may be explained by the time needed for the pollutant (NO) to be completely degraded at the surface of the photocatalyst. The kinetic of the PCO process is linked to a phenomenon called residence time, also known as "space time", defined as the total volume of the reactor divided by the volumetric gas flow rate. At higher flow rates, the residence time of pollutants on the photocatalyst surface becomes shorter which eventually is not enough to induce a complete conversion thereby forming a by-product. A too short residence time of pollutant is usually problematic for air purification systems since it influences greatly the number of available molecules which can be adsorbed to the active sites of a photocatalyst [49,50]. As shown in Eq. (9), NO can only form one stable intermediate, NO_2 (since HNO_2 is very unstable and will react as soon as it has been formed), which is extremely harmful to humans being even at ppb level [51].

In this study, the photocatalyst is well dispersed at the WWCB's surface but it also covers strands deep inside the composite material, as characterized by EDX (Fig. 7). Since this substrate has an open and porous structure, the pollutant, carried by the air flow, can reach most of the activated sites with an adequate residence time allowing a complete NO conversion to NO_3^-. AAC has a higher surface area and its pits are well dispersed at the surface, ensuring a good PCO efficiency, but they are not interconnected, contrary to the WWCB. Moreover, these pits have a small diameter, averaging 1.2 mm which is two times narrower than the WWCB ones. It may explain that at high flow rate, the air flow cannot properly stream inside the pits resulting in low residence time of the pollutants.

This phenomenon will be further studied by doing a CFD simulation of the air/pollutant flow through the two substrates.

3.4. Simulation of the velocity development of the flow

The air flow at the surface of the two substrates at different flow rates are shown in Figs. 12 and 13. It appears that the air/pollutant flow is mostly located at the AAC's surface whereas it can enter inside the WWCB. Therefore, the morphology of the two substrates does have an impact on the air flow.

The first noticeable difference between the two substrates is the pore size, which is almost two times bigger for the WWCB (d = 2.6 mm) than for the AAC (d = 1.2 mm). Thus, the air/pollutant flow can penetrate more easily inside the WWCB than the AAC. It means that even though the photocatalyst is also deposited at the bottom of the AAC's pores, as it has been characterized in Fig. 6B and Fig. 8, the air/pollutant flow cannot reach this region if the pore is too deep. Indeed, the CFD simulation shows that the flow becomes insignificant if the pore is deeper than 0.5 mm.

Another dissimilarity between the two substrates is their morphology and their type of porosity. WWCB has an open-pore structure whereas AAC has a close-pore structure. It means that the interconnection between the WWCB's pores allows the air to flow through the material, which is confirmed by the CFD simulation. Moreover, inside the WWCB, the flow is significantly lower, allowing a residence

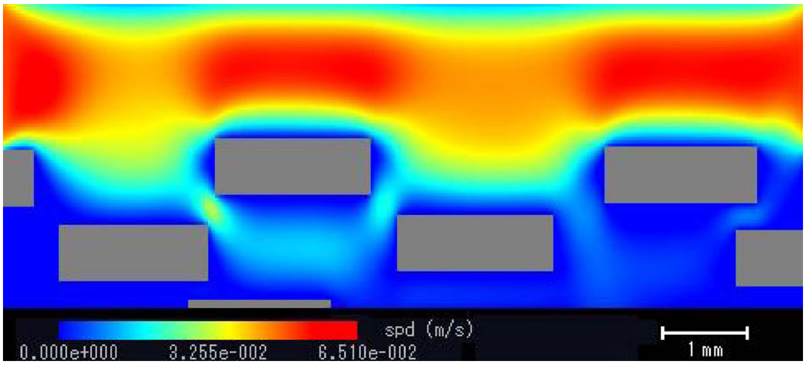

Fig. 12. CFD simulation of WWCB. Air flow is set at 1 L/min.

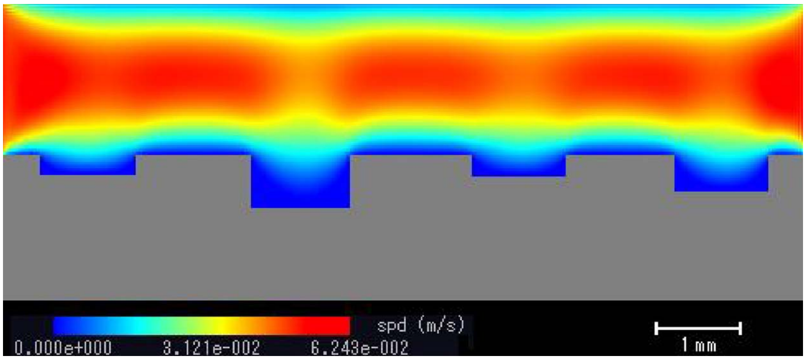

Fig. 13. CFD simulation of AAC. Air flow is set at 1 L/min.

time of the pollutants at the photocatalyst surface long enough to guarantee a complete conversion. This phenomenon can explain the low NO_2 release of this material: Indeed, even at a higher flow rate, this flow would stream through the material at a reduced speed. On the other hand, with AAC, the main stream mostly flows at the substrate's surface (since it cannot properly flow through pores) and at a higher flow rate, the residence time at the surface is not long enough to promote a complete NO degradation, explaining the significant amount of NO_2 released.

4. Conclusion

In this study, two different porous substrates are used as photocatalyst carriers. Their morphology and physical properties are characterized and compared prior to the study of the photocatalytic oxidation efficiency of NO with these substrates. The following conclusions can be drawn from the present study:

- Characterization of the substrates highlights the different structures of the two materials. WWCB has an open-pore structure with high roughness depth (4.25 mm) whereas AAC has a closed-pore structure and a low roughness depth (0.57 mm). Besides, the presence of micropores (averaging 1 µm) at the surface of AAC provides a higher effective area, even though the surface area of both substrates are comparable.
- Photocatalytic efficiency assessment shows that both materials are outstanding candidates as photocatalyst carrier since they show up to 98% of NO_x degradation efficiency.
- The high effective area of AAC increases the activated sites which initiate the PCO process, resulting in higher NO degradation. However, AAC also releases an important amount of NO_2 (up to 12%) because of its closed-pores structure.
- The presence of an open-pore structure of the WWCB favors a longer residence time, limiting the production and release of NO_2. Moreover, the air flow rate has a little impact on PCO efficiency of substrates with substrates with open porosity such as WWCB.
- CFD simulation confirms the importance of the pore structure on PCO efficiency. The open-pore structure of WWCB promotes air stream through the substrate, more than the AAC closed structure, allowing a complete NO conversion into NO_3^-.

Acknowledgments

The authors would like to acknowledge the financial support provided by STW (Stichting voor de Technische Wetenschappen), the Netherlands, as this work is included in the project “Development of sustainable and functionalized inorganic binder-biofiber composites”, project number 10013077. For the materials, the authors would like to acknowledge Knauf insulation, Kronos, and Joma. For the equipment support, the authors would like to acknowledge Ir. Simon Hermans (Keyence Microscope Europe). Furthermore, the authors wish to express their gratitude to Guillaume Doudart de la Gree for the valuable discussions, concerning the wood wool features and properties, involving the photo-catalytic degradation.

References

[1] A.P. Jones, Indoor air quality and health, Atmos. Environ. 33 (1999) 4535–4564, http://dx.doi.org/10.1016/S1352-2310(99)00272-1.
[2] Guidance Notes for the Management of Indoor Air Quality in Offices and Public Places, Indoor Air Quality Management Group, 2003.
[3] K. Partti-Pellinen, O. Marttila, A. Ahonen, O. Suominen, T. Haahtela, Penetration of nitrogen oxides and particles from outdoor into indoor air and removal of the pollutants through filtration of incoming air, Indoor Air 10 (2000) 126–132, http://dx.doi.org/10.1034/j.1600-0668.2000.010002126.x.
[4] M.M. Ballari, Q.L. Yu, H.J.H. Brouwers, Experimental study of the NO and NO2 degradation by photocatalytically active concrete, Catal. Today 161 (2011) 175–180, http://dx.doi.org/10.1016/j.cattod.2010.09.028.
[5] B.C. Faust, M.R. Hoffmann, D.W. Bahnemann, Photocatalytic oxidation of sulfur dioxide in aqueous suspensions of α-Fe2O3, J. Phys. Chem. 93 (1989) 6371–6381, http://dx.doi.org/10.1021/j100354a021.
[6] M. Sleiman, P. Conchon, C. Ferronato, J.M. Chovelon, Photocatalytic oxidation of toluene at indoor air levels (ppbv): towards a better assessment of conversion, reaction intermediates and mineralization, Appl. Catal. B Environ. 86 (2009) 159–165, http://dx.doi.org/10.1016/j.apcatb.2008.08.003.
[7] J. Zhao, X. Yang, Photocatalytic oxidation for indoor air purification: a literature review, Build. Environ. 38 (2003) 645–654, http://dx.doi.org/10.1016/S0360-1323(02)00212-3.
[8] M.M. Ballari, H.J.H. Brouwers, Full scale demonstration of air-purifying pavement, J. Hazard. Mater. 254–255 (2013) 406–414, http://dx.doi.org/10.1016/j.jhazmat.2013.02.012.
[9] C.H. Ao, S.C. Lee, C.L. Mak, L.Y. Chan, Photodegradation of volatile organic compounds (VOCs) and NO for indoor air purification using TiO2: promotion versus inhibition effect of NO, Appl. Catal. B Environ. 42 (2003) 119–129, http://dx.doi.org/10.1016/S0926-3373(02)00219-9.
[10] Z. Ding, G.Q. Lu, P.F. Greenfield, Role of the crystallite phase of TiO2 in heterogeneous photocatalysis for phenol oxidation in water, J. Phys. Chem. 104 (19) (2000), http://dx.doi.org/10.1021/JP993819B.
[11] Z. Ji, X. Jin, S. George, T. Xia, H. Meng, X. Wang, E. Suarez, H. Zhang, E.M.V. Hoek, H. Godwin, A.E. Nel, J.I. Zink, Dispersion and stability optimization of TiO2 nanoparticles in cell culture media, Environ. Sci. Technol. 44 (2010) 7309–7314, http://dx.doi.org/10.1021/es100417s.
[12] M.R. Hoffmann, S.T. Martin, W. Choi, D.W. Bahnemann, Environmental applications of semiconductor photocatalysis, Chem. Rev. 95 (1995) 69–96, http://dx.doi.org/10.1021/cr00033a004.
[13] C. Di Valentin, G. Pacchioni, Trends in non-metal doping of anatase TiO2: B, C, N and F, Catal. Today 206 (2013) 12–18, http://dx.doi.org/10.1016/j.cattod.2011.11.030.
[14] A. Zaleska, Doped-TiO2: A Review, Recent Patents Eng. 2 (2008) 157-164. 10.2174/187221208786306289.
[15] J.M. Coronado, F. Fresno, M.D. Hernández-Alonso, R. Portela, Design of Advanced Photocatalytic Materials for Energy and Environmental Applications, (2013), http://dx.doi.org/10.1007/978-1-4471-5061-9.
[16] A.A. Daniyan, L.E. Umoru, B. Olunlade, Preparation of nano-TiO 2 thin film using spin coating method, J. Miner. Mater. Charact. Eng. 1 (2013) 138–144, http://dx.doi.org/10.4236/jmmce.2013.14024.
[17] N. Negishi, K. Takeuchi, T. Ibusuki, Preparation of the TiO 2 thin film photocatalyst by the dip-coating process, J. Sol-Gel Sci. Technol. 19 (1998) 43–691.
[18] F. Wang, B. Qi, G. Wang, W. Cui, Catalyst coating deposition behavior by cold spray for fuel reforming, Int. J. Hydrogen Energy (2014) 13852–13858, http://dx.doi.org/10.1016/j.ijhydene.2014.01.133.
[19] Q.L. Yu, M.M. Ballari, H.J.H. Brouwers, Indoor air purification using heterogeneous photocatalytic oxidation. Part II: Kinetic study, Appl. Catal. B Environ. 99 (2010) 58–65, http://dx.doi.org/10.1016/j.apcatb.2010.05.032.
[20] Kuo-Hua Wang, Huan-Hung Tsai, Yung-Hsu Hsieh, A study of photocatalytic degradation of trichloroethylene in vapor phase on TiO2 photocatalyst, Chemosphere

36 (1998) 2763–2773, http://dx.doi.org/10.1016/S0045-6535(97)10235-1.

[21] C.H. Ao, S.C. Lee, Enhancement effect of TiO2 immobilized on activated carbon filter for the photodegradation of pollutants at typical indoor air level, Appl. Catal. B Environ. 44 (2003) 191–205, http://dx.doi.org/10.1016/S0926-3373(03)00054-7.

[22] ISO, ISO 22197-1 — Test Method for Air-purification Performance of Semiconducting Photocatalytic Materials — Part 1: Removal of Nitric Oxide, (2016).

[23] M. Hunger, G. Hüsken, H.J.H. Brouwers, Photocatalysis applied to concrete products, Zkg Int. 61 (2008) 77–85.

[24] P. Spiesz, P. Buluk, Q.L. Yu, Enhanced air pollutant removal efficiency of photocatalytic concrete with waste glass, NTCC 2014 Int. Conf. Non-Traditional Cem. Concr. (2014) 5–8.

[25] Š. Lorenčik, Q.L. Yu, H.J.H. Brouwers, Indoor air purification using functional wall covering, Proc. 18th Int. Conf. Build. Mater. (Ibausil), Weimar, 2012.

[26] T. Martinez, A. Bertron, E. Ringot, G. Escadeillas, Degradation of NO using photocatalytic coatings applied to different substrates, Build. Environ. 46 (2011) 1808–1816, http://dx.doi.org/10.1016/j.buildenv.2011.03.001.

[27] Š. Lorenčik, Q.L. Yu, H.J.H. Brouwers, Design and performance evaluation of the functional coating for air purification under indoor conditions, Appl. Catal. B Environ. 168–169 (2015) 77–86, http://dx.doi.org/10.1016/j.apcatb.2014.12.012.

[28] A. Rachel, B. Lavedrine, M. Subrahmanyam, P. Boule, Use of porous lavas as supports of photocatalysts, Catal. Commun. 3 (2002) 165–171, http://dx.doi.org/10.1016/S1566-7367(02)00076-6.

[29] F. Wang, L. Yang, G. Sun, L. Guan, S. Hu, The hierarchical porous structure of substrate enhanced photocatalytic activity of TiO2/cementitious materials, Constr. Build. Mater. 64 (2014) 488–495, http://dx.doi.org/10.1016/j.conbuildmat.2014.04.073.

[30] C.M.A. Parlett, K. Wilson, A.F. Lee, Hierarchical porous materials: catalytic applications, Chem. Soc. Rev. 42 (2013) 3876–3893, http://dx.doi.org/10.1039/C2CS35378D.

[31] Y. Zhang, E.K. Stefanakos, D. Yogi Goswami, Effect of photocatalytic surface roughness on reactors effectiveness for indoor air cleaning, Build. Environ. 61 (2013) 188–196, http://dx.doi.org/10.1016/j.buildenv.2012.12.018.

[32] K. Kochova, Use of alternative fibres in Wood Wool cement boards and their influence on cement hydration, 19th Int. Conf. Build. Mater. Ibausil, 2015, pp. 1372–1375 https://pure.tue.nl/ws/files/3889104/935776505712757.pdf.

[33] A.A. Moslemi, S.C. Pfister, The influence of cement wood ratio and cement type on Bending strength and dimensional stability of wood-Cement composite panels, Wood Fiber Sci. 19 (1987) 165–175.

[34] S. Frybort, R. Mauritz, A. Teischinger, U. Müller, Cement bonded composites – A mechanical review, BioResources 3 (2) (2008) 602–626.

[35] A. Bouguerra, A. Ledhem, F. De Barquin, R. Dheilly, M. Quéneudec, Effect of microstructure on the mechanical and thermal properties of lightweight concrete prepared from clay, cement, and wood aggregates, Cem. Concr. Res. 28 (8) (1998) 1179–1190.

[36] R.W. Wolfe, A. Gjinolli, Durability and strength of cement-bonded wood particle composites made from construction waste, For. Prod. J. (February (49)) (1999).

[37] B. Goodell, G. Daniel, J. Liu, L. Mott, R. Frank, Decay resistance and microscopic analysis of wood-cement composites, For. Prod. J. 47 (11–12) (1997) 75–80.

[38] E. Johansson, Woodwool slabs – production, properties and use, Build. Issues (1994), http://www.lunduniversity.lu.se/o.o.i.s?id=12683&postid=4354267.

[39] N. Narayanan, K. Ramamurthy, Structure and properties of aerated concrete: a review, Cem. Concr. Compos. 22 (2000) 321–329, http://dx.doi.org/10.1016/S0958-9465(00)00016-0.

[40] A. Hauser, U. Eggenberger, T. Mumenthaler, Fly ash from cellulose industry as secondary raw material in autoclaved aerated concrete, Cem. Concr. Res. 29 (1999) 297–302, http://dx.doi.org/10.1016/S0008-8846(98)00207-5.

[41] A.M. Ramirez, K. Demeestere, N. De Belie, T. Mäntylä, E. Levänen, Titanium dioxide coated cementitious materials for air purifying purposes: preparation, characterization and toluene removal potential, Build. Environ. 45 (2010) 832–838, http://dx.doi.org/10.1016/j.buildenv.2009.09.003.

[42] A. Maury-Ramirez, K. Demeestere, N. De Belie, Photocatalytic activity of titanium dioxide nanoparticle coatings applied on autoclaved aerated concrete: effect of weathering on coating physical characteristics and gaseous toluene removal, J. Hazard. Mater. 211–212 (2012) 218–225, http://dx.doi.org/10.1016/j.jhazmat.2011.12.037.

[43] S. Laufs, G. Burgeth, W. Duttlinger, R. Kurtenbach, M. Maban, C. Thomas, P. Wiesen, J. Kleffmann, Conversion of nitrogen oxides on commercial photocatalytic dispersion paints, Atmos. Environ. 44 (2010) 2341–2349, http://dx.doi.org/10.1016/j.atmosenv.2010.03.038.

[44] Y. Ohko, Y. Nakamura, N. Negishi, S. Matsuzawa, K. Takeuchi, Photocatalytic oxidation of nitrogen monoxide using TiO2 thin films under continuous UV light illumination, J. Photochem. Photobiol. A Chem. 205 (2009) 28–33, http://dx.doi.org/10.1016/j.jphotochem.2009.04.005.

[45] Y. Ohko, Y. Nakamura, N. Negishi, S. Matsuzawa, K. Takeuchi, Unexpected release of HNO3 and related species from UV-illuminated TiO2 surface into air in photocatalytic oxidation of NO2, Environ. Chem. Lett. 8 (2010) 289–294, http://dx.doi.org/10.1007/s10311-009-0219-9.

[46] A. Gandolfo, V. Bartolomei, E. Gomez Alvarez, S. Tlili, S. Gligorovski, J. Kleffmann, H. Wortham, The effectiveness of indoor photocatalytic paints on NOx and HONO levels, Appl. Catal. B Environ. 166–167 (2015) 84–90, http://dx.doi.org/10.1016/j.apcatb.2014.11.011.

[47] N. Narayanan, K. Ramamurthy, Structure and properties of aerated concrete: a review, Cem. Concr. Compos. 22 (2000) 321–329, http://dx.doi.org/10.1016/S0958-9465(00)00016-0.

[48] E. Boonen, A. Beeldens, Recent photocatalytic applications for air purification in Belgium, Coatings 4 (2014) 553–573, http://dx.doi.org/10.3390/coatings4030553.

[49] J. Lv, L. Zhu, Highly efficient indoor air purification using adsorption-enhanced-photocatalysis-based microporous TiO 2 at short residence time, Environ. Technol. 34 (2013) 1447–1454, http://dx.doi.org/10.1080/09593330.2012.752875.

[50] O. Levenspiel, Chemical Reaction Engineering, John Wiley & Sons, 1999, http://dx.doi.org/10.1021/ie990488g.

[51] T.W. Hesterberg, W.B. Bunn, R.O. McClellan, A.K. Hamade, C.M. Long, P.A. Valberg, Critical review of the human data on short-term nitrogen dioxide (NO2) exposures: evidence for NO2 no-effect levels, Crit. Rev. Toxicol. 39 (2009) 743–781, http://dx.doi.org/10.3109/10408440903294945.